Optimizing silicon doping levels for enhanced osteogenic and angiogenic properties of 3D-printed biphasic calcium phosphate scaffolds: An *in vitro* screening and *in vivo* validation study

Teliang Lu [a,b,1], Guohao Li [c,e,1], Luhui Zhang [a], Xinyuan Yuan [a], Tingting Wu [b,**], Jiandong Ye [a,d,*]

[a] *School of Materials Science and Engineering and Key Laboratory of Biomedical Materials of Ministry of Education, South China University of Technology, Guangzhou, 510641, PR China*
[b] *National Engineering Research Center for Healthcare Devices, Guangdong Key Lab of Medical Electronic Instruments and Polymer Material Products, Institute of Biological and Medical Engineering, Guangdong Academy of Sciences, Guangzhou, Guangdong, 510316, PR China*
[c] *The Third Affiliated Hospital of Southern Medical University, Guangzhou, Guangdong, 510630, PR China*
[d] *National Engineering Research Center for Tissue Restoration and Reconstruction, Guangzhou, 510006, PR China*
[e] *Zhoukou Center Hospital, Zhoukou, Henan, 466000, PR China*

ARTICLE INFO

ABSTRACT

Biphasic calcium phosphate (BCP) ceramics are valued for their osteoconductive properties but have limited osteogenic and angiogenic activities, which restricts their clinical utility in bone defect repair. Silicon doping has emerged as an effective strategy to enhance these biological functions of BCP. However, the biological impact of BCP is influenced by the level of silicon doping, necessitating determination of the optimal concentration to maximize efficacy in bone repair. This study investigated the effects of silicon doping on both the physico-chemical and biological properties of BCP, with a specific focus on osteogenic and angiogenic potentials. Results indicated that silicon doping exceeding 4 mol.% led to the formation of α-TCP, accelerating BCP degradation, enhancing silicon ion release, and promoting mineralization product formation. Simultaneously, silicon doping increased the porosity of BCP scaffolds, which typically reduces their compressive strength. Nevertheless, scaffolds doped with ≤4 mol.% silicon maintained compressive strengths exceeding 2 MPa. *In vitro* biological experiments indicated that higher levels of silicon doping (≥6 mol.%) partially inhibited the successful differentiation of stem cells and the vascularization of endothelial cells. Optimal conditions for promoting osteogenic differentiation and angiogenesis were identified between 2 and 4 mol.% silicon doping, with an optimal level of approximately 4 mol.%. Subsequent *in vivo* experiments confirmed that BCP scaffolds doped with 4 mol.% silicon effectively promoted vascularization and new bone formation, highlighting their potential for clinical bone defect repair.

1. Introduction

The repair of bone defects has long been a prominent issue in the medical field, given the substantial adverse effects on patients' lives and health resulting from bone defects caused by factors such as accidents, diseases, or aging [1,2]. Traditional autologous or allogeneic bone transplantation is constrained by various limitations, including limited sources of autologous bone grafts, significant risks of immune rejection with allogeneic bone grafts, and instability in repair outcomes [3,4]. Consequently, there is an urgent need to identify a safe and effective alternative approach. Calcium phosphate materials are favored for their similar chemical composition to human tissues and good biocompatibility [5]. Among them, biphasic calcium phosphate (BCP) is an important ceramic material, combining hydroxyapatite (HA) and

---

beta-tricalcium phosphate (β-TCP) with two different crystal phases, exhibiting excellent bioactivity and mechanical properties [6,7]. In contrast to pure HA and β-TCP, the degradation rate of BCP can be controlled by altering its phase composition. This capability allows for matching the degradation rate of BCP with the ingrowth of new bone tissue, thereby enhancing the effectiveness of bone defect repair [8].

Nevertheless, BCP still exhibits limitations as a bone repair material, particularly in terms of its relatively low osteogenic and angiogenic activities [9,10]. To address these challenges, researchers have turned their attention to enhancing the biological activity of BCP through active ion doping [11,12]. Zinc, magnesium, strontium, and silicon are among the most extensively studied osteogenic dopants. Studies have indicated that zinc [13,14], magnesium [15], and strontium [16] doping can enhance the osteogenic capability of BCP ceramic scaffolds. However, the introduction of zinc and magnesium ions tends to increase the sintered density of BCP ceramic scaffolds, thereby potentially reducing scaffold degradation rates to varying extents [11,17], which may hinder the material's replacement by new bone tissue. On the other hand, strontium doping can increase the degradation rate of BCP ceramics [16], but optimal strontium doping levels have not been systematically explored.

Among the various doping elements, silicon has garnered attention for its significant role in bone tissue regeneration. It is commonly found in bone tissue and at bone-bone interfaces [18], promoting cartilage and glycosaminoglycans synthesis and functionalization, benefiting cardiovascular health and defect repair [19]. Research has demonstrated that silicon promotes angiogenesis by stimulating endothelial cells to secrete vascular endothelial growth factor (VEGF), enhancing the synthesis of endothelial nitric oxide synthase (eNOS) and nitric oxide (NO), thereby facilitating the formation and maturation of new blood vessels [20,21]. In addition, silicon doping has been shown to accelerate the bone defect repair rate of calcium phosphate scaffolds [22,23].

However, excessive silicon doping may lead to adverse effects, including the generation of α-TCP [24] and the release of high concentrations of silicon ions, which inhibit osteogenic and angiogenic activities [25,26]. This highlights the importance of determining the optimal amount of silicon doping to enhance the effectiveness of BCP in bone defect repair. However, research on this issue is currently lacking and requires further in-depth exploration and empirical studies.

In this study, we employed the chemical precipitation method to prepare BCP powders with varying levels of silicon doping, followed by the fabrication of ceramic scaffolds with a three-dimensional interconnected macroporous structure using extrusion-based 3D printing technology. The primary focus was on investigating the influence of silicon doping on the physicochemical properties and biological properties of BCP, including its osteogenic and angiogenic capabilities. Cell culture experiments were employed to identify the most favorable range of silicon doping for promoting osteogenic differentiation of stem cells and angiogenesis of endothelial cells. Ultimately, silicon-doped BCP ceramic scaffolds were implanted into animal models to verify their impact on *in vivo* bone and vessel formation, thereby providing a theoretical and practical basis for the application of BCP in bone defect repair.

2. Experiment section

2.1. Materials

Ca(NO₃)₂·4H₂O, (NH₄)₂HPO₄, and NH₄OH solution (25 %) were procured from Guangzhou Chemical Reagent Factory (China). Tetraethyl orthosilicate (TEOS) was sourced from Aladdin (China). Penicillin/streptomycin and fetal bovine serum (FBS) were obtained from Biological Industries (Israel). Dulbecco's modified eagle's medium (DMEM) was provided by Gibco (USA). Cell counting kit-8 (CCK8) solution and Live/Dead staining solution were purchased from Dojindo (Japan) and Biotium (USA), respectively. Trypsin, micro BCA protein

assay kit, and forward-reverse primers were sourced from Thermo Scientific (USA). Sodium β-glycerophosphate, dexamethasone, vitamin C, and disodium 4-nitrophenylphosphate (pNPP) were purchased from Sigma-Aldrich. RIPA lysis buffer and BCIP/NBT alkaline phosphatase (ALP) color development kit were provided by Biyotime (China). SYBR agent and a Transcriptor First Strand cDNA Synthesis Kit were obtained from Roche (Germany).

2.2. Synthesis of silicon doping biphasic calcium phosphate (Si-BCP) powder

Silicon-doped BCP powder was synthesized using a chemical precipitation method. In a nutshell, solutions of (NH₄)₂HPO₄ (0.6 mol/L) and Ca(NO₃)₂·4H₂O (1 mol/L) were prepared separately, along with a P + Si mixture solution containing (NH₄)₂HPO₄ and tetraethyl orthosilicate (TEOS) at varying silicon molar percentages. The total concentration of the P + Si solution was maintained at 0.6 mol/L, and the Ca/(P + Si) molar ratio was held constant at 1.67. Subsequently, either the (NH₄)₂HPO₄ solution or the P + Si mixture solution was introduced into the Ca(NO₃)₂·4H₂O solution using a peristaltic multi-channel pump under continuous stirring, as detailed in Table S1 regarding specific reaction volumes. Following this, NH₄OH solution was added to adjust the pH of the mixture to 10.2. The resulting solution underwent continuous stirring for 2 h, followed by aging for 24 h. The resultant paste underwent washing thrice with deionized water and once with ethanol, followed by lyophilization. After lyophilization, the powder was subjected to calcination in a furnace at different temperatures (900, 1000, and 1100 °C) for 2 h, with a heating and cooling rate of 5 °C/min. The calcined powder was then sieved to a particle size below 53 μm for subsequent use.

2.3. Characterization of Si-BCP powder

The crystal structure and phase composition of the silicon-doped BCP (Si-BCP) powder were characterized using X-ray diffraction (XRD) analysis performed on an X'Pert instrument from PANalytical in the Netherlands. CaKα radiation with a wavelength (λ) of 1.5418 Å, operated at 40 kV and 40 mA, was utilized for the analysis. XRD data were collected over a 2θ range of 10°–70° with a step size of 0.013° and a duration time of 30 s. Rietveld refinements of the X-ray diffraction patterns were conducted for each sample using the GSAS software, employing the structural models of hydroxyapatite (HA), β-tricalcium phosphate (β-TCP), and α-tricalcium phosphate (α-TCP) from the corresponding Powder Diffraction File (PDF) numbers: #090432, #090169, and #090348, respectively.

Furthermore, elemental analysis of the samples was carried out using X-ray photoelectron spectroscopy (XPS; K-Alpha, Thermo Fisher Scientific, USA) with Al Kα radiation. The Si-BCP powder samples were pelletized with potassium bromide (KBr) and subjected to Fourier transform infrared (FTIR) spectroscopy using a Vector 33-MIR spectrometer by Bruker Optik in Germany. Raman spectral analysis was conducted utilizing a Smart Raman Spectrometer (LabRAM Aramis, HORIBA Jobin Yvon, France). The vibrational modes of phosphate and hydroxyl stretching were investigated by recording spectra in the frequency ranges of 100–1600 cm⁻¹ and 3500-3650 cm⁻¹, respectively.

2.4. Preparation of powder extracts

The powder extracts were prepared in accordance with the protocols outlined in the International Standard Organization (ISO) 10993-12. Briefly, Si-BCP powder, subjected to a 2-h treatment at 900 °C, was immersed in DMEM at 37 °C, with a powder mass to medium volume ratio of 0.2 g/mL. Following a 24-h incubation period, the mixtures were centrifuged, and the supernatant was collected. Subsequently, the collected extracts were filtered through 220 nm filtering membranes for sterilization.

2.5. In vitro biocompatibility and osteogenic differentiation

2.5.1. Stem cell cultivation

In this experiment, mouse bone mesenchymal stem cells (mBMSCs, obtained from ATCC, USA) at passage 6 were employed. The mBMSCs were utilized to investigate the *in vitro* cell biocompatibility, proliferation, and osteogenic activities of Si-BCP powders and Si-BCP extracts. For cell culture, a cell culture medium (complete culture medium) consisting of DMEM with 10 vol% fetal bovine serum (FBS) was employed. Furthermore, the osteogenic induction medium was supplemented with 10 mM sodium β-glycerophosphate, 0.1 μM dexamethasone, and 50 mg/L vitamin C.

2.5.2. Cell proliferation

A volume of 200 μL of mBMSCs suspension at a concentration of 1×10^4 cells/mL was plated in a 96-well plate and cultured for 24 h. Subsequently, the cell medium was replaced with either extract medium or a suspension of Si-BCP powder (10 mg/L) containing 10 vol% FBS. Stem cells cultured in powder extract were replenished with fresh extract every two days, while those directly co-cultured with powder were refreshed with complete culture medium every two days. Following 1, 2, and 4 days of culture, the cell medium was aspirated, and 100 μL of CCK8 working solution was added, followed by an incubation at 37 °C for 1 h. The quantification of cell proliferation was conducted by measuring the absorbance at 450 nm using an ELISA reader (Thermo 3001, Thermo, USA).

2.5.3. Live/dead staining

For cell viability, cells cultured for 2 days for live/dead stain by a Live/Dead staining kit were observed under a fluorescence inverted microscope (Axio Observer 7, ZEISS, Germany).

2.5.4. Alkaline phosphatase (ALP) evaluation

For ALP activity measurement, mBMSCs were seeded at a density of 2×10^4 cells per well in a 48-well plate. After 1 day of culture, the cell medium was replaced with either powder extract medium or a suspension of Si-BCP powder (10 mg/L) supplemented with osteogenic inductive components. Following 3, 7, and 14 days of culture, the culture medium was removed, and the cells were rinsed with cold PBS twice. Subsequently, 300 μL of RIPA lysis buffer solution was added to each well and incubated at 4 °C for 2 h. The total protein content of the lysate was determined using the Micro BCA Protein Assay Kit according to the operation manual. The ALP activity of mBMSCs on the samples was assessed using a p-NPP assay. In this assay, 200 μL of p-NPP solution was added to a 48-well plate along with 20 μL of the lysate and incubated for 15 min. Then, 200 μL of 1 M NaOH solution was added to each well to terminate the reaction. The concentration of p-nitrophenol (p-NP) formed was measured by determining the absorbance at 405 nm. ALP activity was expressed as enzyme activity units per milligram of total protein content. Each sample was tested in six replicates.

2.5.5. ALP staining

The cells were fixed with 4 % glutaraldehyde for 30 min after 7 days of culture. Subsequently, they were stained with ALP using the BCIP/NBT color development kit for morphological observation under a fluorescence inverted microscope.

2.5.6. RT-qPCR analysis

Real-time quantitative polymerase chain reaction (RT-qPCR) method was employed to analyze the expression of osteogenic genes in mBMSCs. The cells were seeded at a density of 2×10^4 cells per well in a 48-well plate. After 7 and 14 days of culture, total RNA was extracted using the Hipure Total RNA Micro Kit (Magen, China) and reverse transcribed into complementary DNA using the Transcriptor First Strand cDNA Synthesis Kit. PCR assays to determine the expression of osteogenic activity-related genes were performed using the Applied BiosystemsTM

QuantStudioTM 6 Flex (Thermo Fisher Scientific, USA). The osteogenesis-related genes included runt-related transcription factor 2 (Runx2), collagen type I (Col-I), ALP, osteopontin (OPN), bone sialoprotein (BSP), and osteocalcin (OCN), with glyceraldehyde phosphate dehydrogenase (GAPDH) used as the housekeeping gene. The primer sequences for the genes are provided in Table S2. The relative gene expression was calculated using $2^{-\Delta\Delta Ct}$, where Ct represents the cycle number at which an arbitrarily placed threshold was reached, $\Delta Ct = Ct$ (target gene) – Ct (GAPDH), and $\Delta\Delta Ct =$ sample group [Ct (target gene) – Ct (GAPDH)] - control group [Ct (target gene) – Ct (GAPDH)].

2.5.7. Western blot analysis

Proteins from mBMSCs were isolated using cell lysis buffer (Beyotime, China), and their total concentrations were determined using a BCA protein assay kit (Beyotime, China). Equal amounts of protein extracts were diluted in sample buffer, subjected to 15 % SDS-PAGE, and subsequently transferred onto PVDF membranes. Non-specific binding sites were blocked with 1 % w/v BSA in phosphate-buffered saline (PBST) for 1 h at room temperature. Immunoblotting was performed using antibodies purchased from Affinity. Specifically, the samples were immunoblotted overnight at 4 °C with primary antibodies against GAPDH (1:1500 dilution), Runx2 (1:5000 dilution), Col-I (1:1500 dilution), BSP (1:1500 dilution), and OCN (1:1500 dilution). After washing three times with PBST, the PVDF membrane was incubated with secondary antibodies for 40 min at room temperature. Target proteins were detected using a Luminescent Immunoanalyzer.

2.6. Fabrication and evaluation of Si-BCP scaffolds

Si-BCP scaffolds were fabricated using extrusion-based three-dimensional (3D) printing on the 3D Bio-Architectwork station in Hangzhou, China. The ceramic paste was prepared by blending 8 g of Si-BCP powder with 7 g of 8 wt% polyvinyl alcohol (PVA) solution, followed by mechanical stirring for 3 min. Scaffold models of desired dimensions were designed using computer-aided design (CAD). The paste was extruded through a plastic nozzle with an inside diameter of 400 μm, with an 800 μm strand interval, and then dried at room temperature for 2 days to obtain scaffold preforms. To remove the α-TCP from the Si-BCP preforms, they were transferred to a hydrothermal reactor with a 0.1 M calcium chloride solution as the hydrothermal solvent and treated at 120 °C for 12 h. Subsequently, the hydrothermally treated samples underwent sintering at 1100 °C for 2 h to yield the final Si-BCP ceramic scaffolds.

The characterization of the Si-BCP scaffolds in terms of phase composition, degradation, ion release, and *in vitro* mineralization behavior was conducted as described in the experimental section of the Supporting Information. The proliferation, and osteogenic differentiation of mBMSCs cultured on the scaffold surfaces or in the scaffold extracts were assessed.

2.7. In vitro angiogenesis

Human umbilical vein endothelial cells (HUVECs) were either cultured with scaffolds or in scaffold extracts. After 3 days of culture, the expression levels of angiogenesis-related genes, including hypoxia-inducible factor-1α (HIF-1α), endothelial nitric oxide synthase (eNOS), and vascular endothelial growth factor (VEGF), were assessed using RT-PCR. The primer sequences can be found in Table S3. Furthermore, cells cultured for 3 days were subjected to NO staining, and examined under an inverted fluorescence microscope.

For the tube formation assay, 0.1 mL of medium containing 2×10^4 HUVECs was added to a 48-well plate coated with an extracellular matrix (ECM) layer (Millipore, Germany), followed by the addition of 0.4 mL of scaffold extract. After a 2-h incubation, the tubes formed by migrating HUVECs were visualized using an inverted fluorescence microscope. Image analysis was performed using ImageJ software with the
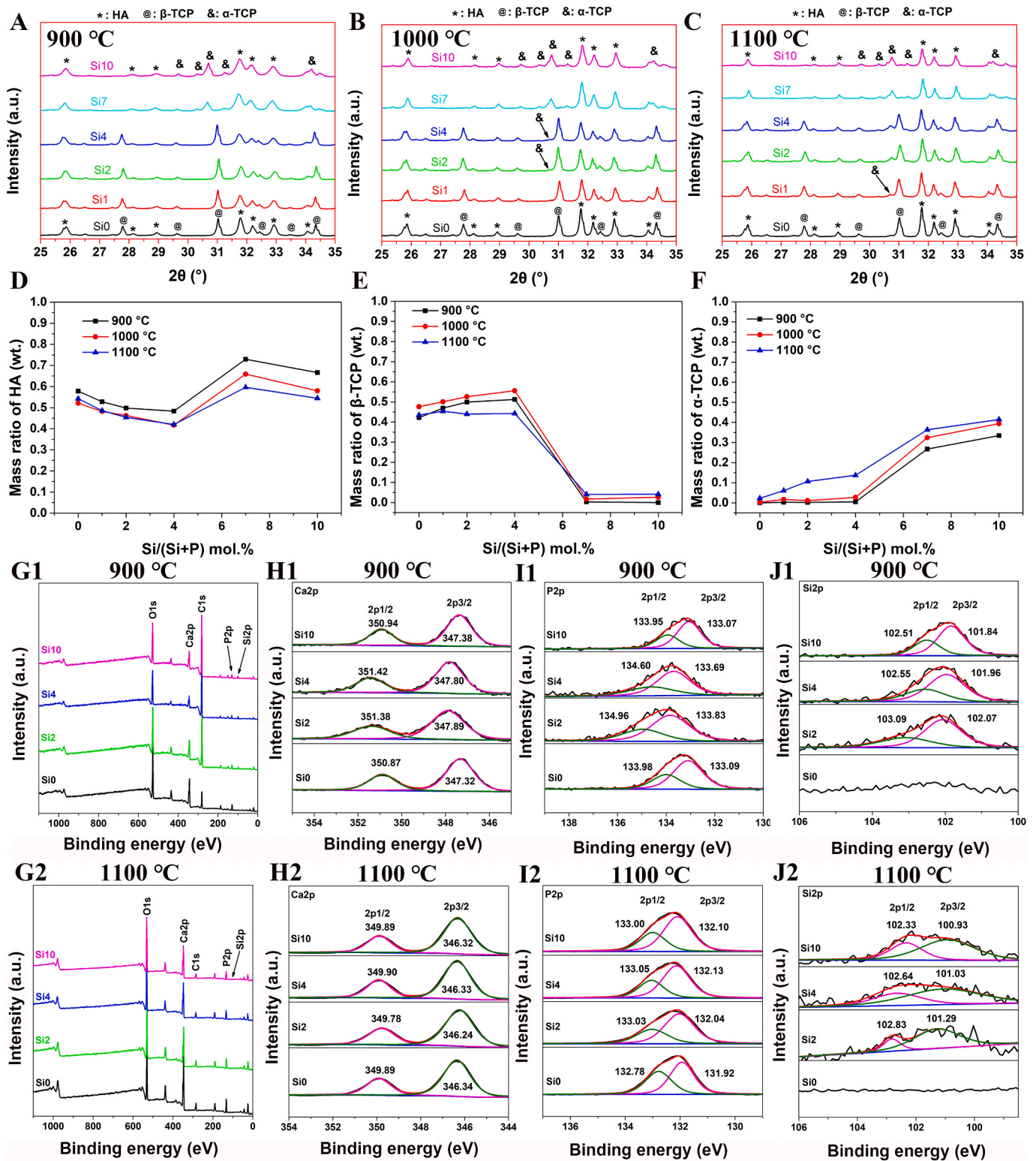
Fig. 1. Composition of Si-doped BCP powder. (A–C) XRD patterns of Si-doped BCP treated at 900 °C, 1000 °C and 1100 °C, respectively; (D–F) Mass ratio of HA, β-TCP and α-TCP in Si-doped BCP powder; (G1, G2) XPS scan spectra and high-resolution spectra of (H1, H2) Ca2p, (I1, I2) P2p, and (J1, J2) Si2p of Si-doped BCP treated at 900 °C and 1100 °C.

Angiogenesis Analyser Plugin to quantify the number of nodes, junctions, and meshes.

Scratch assays were conducted to characterize HUVECs migration. The experimental procedure involved placing a scratch model in the center of a 24-well plate, adding 650 μL of cell suspension (at 3×10^5 cells/mL) into the wells, incubating for 24 h, and then introducing scaffold extract with a serum content of 2 vol%. Photographic observations were made after 0, 12, 24, and 36 h of incubation.
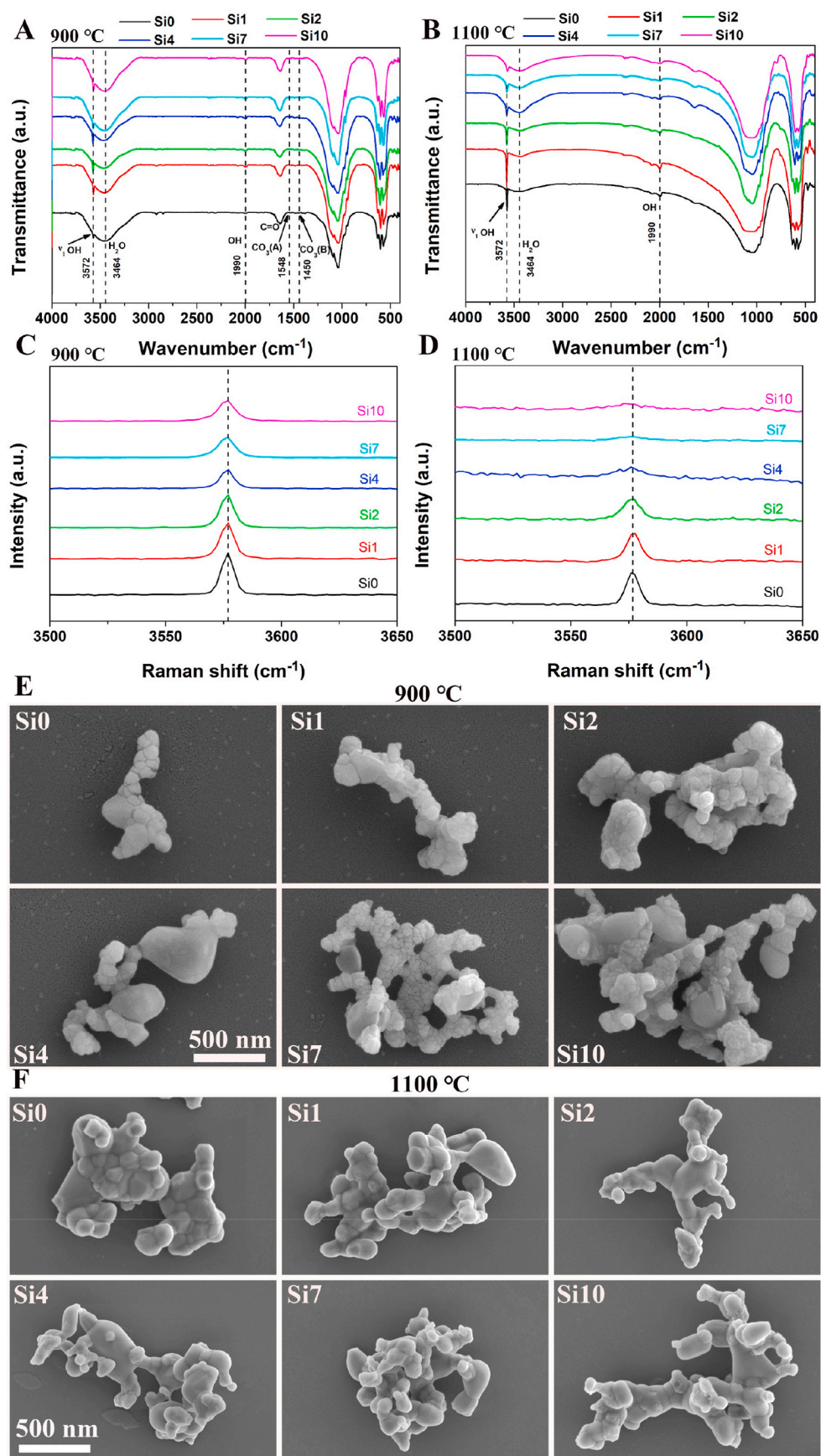
Fig. 2. FTIR spectra at 450-4000 cm^{-1} (A and B), Raman spectra at 3500-3650 cm^{-1} (C and D) and SEM images (E and F) of Si-doped BCP treated at 900 °C and 1100 °C.

2.8. In vivo experiments

2.8.1. In vivo angiogenesis and osteoclasts formation

The animal experiments conducted in this study were carried out in accordance with the guidelines approved by the Ethics Committee of South China University of Technology (ethical code 2019024). Si0–S and Si4–S scaffolds were utilized for the experiment, each having a diameter of 6 mm and a height of 3 mm. These scaffolds were implanted into the abdominal skin of SD rats, with three sets of parallel samples prepared for each scaffold group, and one scaffold implanted per SD rat. After a 7-day post-implantation period, the scaffolds along with the surrounding tissues were retrieved, fixed, decalcified, and embedded in paraffin. Tissue samples were sectioned at a thickness of 5 μm for subsequent analyses.

The assessment of blood vessel generation and development was conducted through immunohistochemical staining of CD31. Furthermore, the impact of the scaffolds on osteoclast formation was evaluated through TRAP staining. Subsequently, the stained samples were visualized using a digital pathology system (P250 Flash, 3D Histech, Hungary) for analysis and documentation.

2.8.2. In vivo bone regeneration evaluation

To assess the *in vivo* bone regeneration potential of Si0–S and Si4–S scaffolds, male New Zealand white rabbits weighing 2.5–3.0 kg were randomly divided into three groups. Two groups received scaffold implants, while the third group served as a control without scaffolds. The scaffolds, with a diameter of 6 mm and a height of 8 mm, were implanted into critical-size bone defects located in the right femoral condyles, with one scaffold per rabbit and three sets of parallel samples prepared for each group. After a 12-week implantation period, the femora containing the implants were collected from the euthanized rabbits.

Microcomputed tomography (micro-CT) imaging (Aloka Latheta LCT-200, HITACHI, Japan) was used for the analysis of the samples. Tissue sections were processed as previously described, stained with hematoxylin and eosin (HE) and Masson's trichrome, and examined using a digital pathology system. The bone regeneration ratio, determined from analysis of HE-stained section images, was quantitatively evaluated using Image-Pro Plus 6.0 software.

2.9. Statistical analysis

Quantitative data are presented as mean ± standard deviations which were obtained from at least 3 replicates. A comparison between two means was made using the Student's *t*-test, with statistical significance set as $p < 0.05$.

3. Result and discussion

3.1. Phase analysis, composition and microstructure

The simplest model for silicon (Si) doping in calcium phosphate (CaP) is the substitution of phosphate (PO_4) with silicate (SiO_4), which results in an asymmetric charge substitution [27]. Typically, this charge neutrality is maintained by generating oxygen vacancies or through excess calcium or hydrogen ions [28,29]. Studies have shown that silicon substitution in calcium phosphate is limited, and only a small amount of silicate ions were found in the lattice of HA with an initial silicon doping content of 4.6 wt% (~10 mol.%) [30]. Therefore, the silicon doping range chosen for this experiment was 0–10 mol.%.

Figure S1 displays the XRD patterns of Si-BCP powder before heat treatment. All the powders showed amorphous peaks corresponding to the characteristic peaks of HA (PDF #090432). The XRD patterns of Si-doped BCP after being calcined at different temperatures for 2 h are presented in Fig. 1A–C. When treated at 900 °C (Fig. 1A), the main phase of samples with a silicon doping content below 4 mol.% was HA and β-TCP, with no α-TCP phases observed. Nevertheless, with silicon doping

levels ≥7 mol.%, there was a notable decrease in the β-TCP phase and a marked increase in the α-TCP phase. When treated at 1000 °C for 2 h (Fig. 1B), a few α-TCP phases were found in Si2 and Si4, and the β-TCP phases disappeared in samples with silicon doping content higher than 7 mol.%. When treated at 1100 °C for 2 h (Fig. 1C), α-TCP was observed in Si1, and the mass ratio of α-TCP increased with an increasing silicon doping content.

The quantitative analysis of phase ratios in samples subjected to heat treatments at 900 °C, 1000 °C, and 1100 °C for 2 h, in relation to silicon doping levels, is depicted in Fig. 1D–F. The proportion of HA by mass (Fig. 1D) exhibited a decreasing trend with rising temperature; within the Si doping range of 0 mol.% to 4 mol.%, the HA mass ratio ranged from 60 wt% to 40 wt%, diminishing with higher silicon content. Regarding the mass proportion of β-TCP (Fig. 1E), it fluctuated between 40 wt% and 60 wt% for Si doping levels ranging from 0 mol.% to 4 mol.%; however, minimal β-TCP was observed beyond 4 mol.% silicon doping, irrespective of the heating temperature. In samples with silicon doping content of 4 mol.% or less, heated below 1100 °C, the α-TCP content remained below 5 wt%. Conversely, as the silicon doping exceeded 4 mol.%, there was a proportional increase in the mass ratio of α-TCP in accordance with the silicon doping levels and treatment temperature. Particularly striking is the finding that Si7 samples treated at 900 °C (as shown in Fig. 1F) exhibited an approximate 25 wt% of α-TCP.

Fig. 1G1-J1 depict the XPS analysis data of Si0, Si2, Si4, and Si10 samples sintered at 900 °C. Analysis of the XPS scan spectra in Fig. 1G1 reveals that the undoped BCP powder (Si0) predominantly comprises C, Ca, P, and O elements. Following silicon doping, a prominent Si2p peak emerges around 102 eV, with the intensity of this peak increasing with higher levels of silicon doping. Fig. 1H1, I1, and J1 display high-resolution spectra of Ca2p, P2p, and Si2p, indicating an overall increase in the binding energy of Ca2p and P2p with silicon doping. Conversely, the binding energy of Si2p decreases as the silicon doping level increases. Upon increasing the sintering temperature to 1100 °C, there were no significant changes observed in the elemental composition of undoped BCP powder and silicon-doped BCP powders (Fig. 1G2). Silicon doping continues to enhance the binding energies of Ca2p (Fig. 1H2) and P2p (Fig. 1I2), while decreasing that of Si2p (Fig. 1J2).

Fig. 2A and B illustrate the FTIR spectra at 450-4000 cm^{-1} of Si-doped samples following a 2-h heat treatment at 900 °C and 1100 °C, respectively. Fig. 2A reveals that all samples exhibit distinct infrared absorption peaks near 3464 cm^{-1}, indicative of the presence of water molecules. Furthermore, absorption peaks corresponding to hydroxyl groups are observed around 3572 and 1900 cm^{-1}, suggesting the existence of HA phases. Additionally, characteristic absorption peaks of both A-type and B-type carbonate ions are detected near 1548 and 1450 cm^{-1}, respectively [31,32]. This observation implies the involvement of atmospheric carbon dioxide during the powder synthesis process. At a sintering temperature of 1100 °C (Fig. 2B), the infrared characteristic peaks of A-type and B-type carbonates become less pronounced or even disappear, indicating decomposition of the carbonate groups within the powder after treatment at 1100 °C.

Figure S2A provides an enlarged view (400-1500 cm^{-1} range) of the FTIR spectra presented in Fig. 2A, specifically focusing on the distinct infrared absorption peaks of phosphate and silicate. The obtained results demonstrate the presence of characteristic absorption peaks associated with phosphate in all samples. Moreover, notable absorption peaks attributed to silicate are observed near 795 and 499 cm^{-1}, predominantly in samples characterized by higher levels of silicon doping, such as Si7 and Si10. Upon increasing the processing temperature to 1100 °C, there were no significant changes observed in the infrared absorption peaks of phosphate and silicate (Figure S2B). This suggests that compared to carbonate ions, phosphate and silicate ions within the powder are more stable and exhibit less variation in response to elevated processing temperatures.

Figures S2C and S2D showcase the Raman spectra at 300-1300 cm^{-1} of Si-doped samples treated at 900 °C and 1100 °C, respectively. As
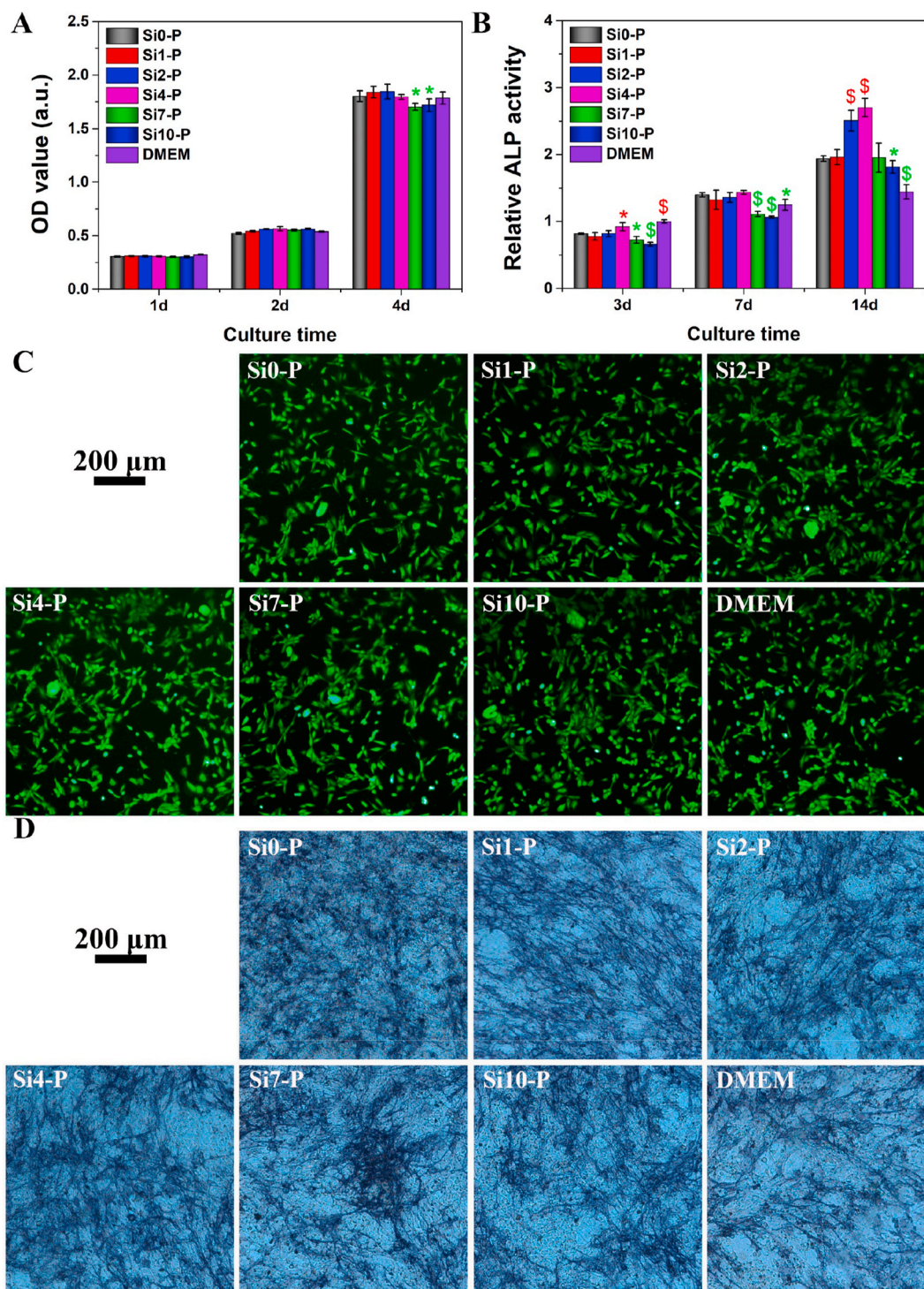
Fig. 3. Cellular response of mBMSCs cultured with Si-doped BCP powders. (A) Cell proliferation; (B) ALP activity; (C) cell viability on day 2; (D) ALP staining on day 7.

depicted in Figure S2C and S2D, the introduction of silicon leads to a reduction in the peak intensity of phosphate around 970 cm^{-1}. Moreover, when the silicon doping concentration exceeds 4 mol.%, the splitting of the primary phosphate peak disappears, likely attributed to the emergence of the α-TCP phase and the concurrent disappearance of the β-TCP phase (see Fig. 1). Within the range of 3500–3650 cm^{-1}, the Raman spectra exhibit characteristic peaks associated with hydroxyl groups (Fig. 2C & D). Notably, an increase in silicon doping concentration results in a decline in the intensity of the hydroxyl feature peak,

accompanied by broadening of the peak width. Moreover, higher sintering temperatures accentuate the broadening of the hydroxyl feature peak. This observation suggests that silicon doping impairs the crystallinity of the HA phase.

SEM images of Si-BCP powders post heat treatment at 900 °C and 1100 °C are displayed in Fig. 2E and F, respectively. The particles treated at 1100 °C show slightly larger dimensions, and various particles with distinct morphologies were observed across all samples, regardless of the treatment temperature. The smaller hexagonal-shaped particles

were identified as HA, while the larger particles corresponded to β-TCP in Si0–Si4 and α-TCP in Si7–10.

3.2. Cell biocompatibility and osteogenic differentiation

The biocompatibility of silicon-doped powders was assessed by evaluating the proliferation of mBMSCs co-cultured with the powders (direct co-culture, Fig. 3) or powder extract (indirect culture, Figure S10) for various durations, along with live/dead staining, using DMEM as a control. Specifically, "Sixx-P″" denotes direct co-culture of stem cells with the powder, while "Sixx-PE" indicates stem cells cultured in the powder extract.

Results from cell proliferation in Fig. 3A indicate that as the incubation period lengthened, cell numbers on the culture plates gradually increased, suggesting normal proliferation of stem cells co-cultured with the powders. However, it is noteworthy that by day 4 of culture, Si7–P and Si10–P showed slight inhibition of stem cell proliferation. Fig. 3C depicts the live/dead staining results of mBMSCs co-cultured with the powders for 2 days, revealing minimal presence of dead cells (stained in red), indicating that silicon-doped powders exhibited no significant cytotoxicity. Additionally, results from co-culturing stem cells with powder extracts also demonstrated no apparent cytotoxicity of silicon-doped powders (Figure S10A and S10C).

The ALP activity of stem cells co-cultured with the powders for 3, 7, and 14 days is illustrated in Fig. 3B. Overall, compared to Si0–P, powders with moderate silicon doping levels such as Si4–P significantly enhance the ALP activity of stem cells, whereas higher levels of doping in Si7–P and Si10–P notably suppress the ALP activity of stem cells. The ALP staining results in Fig. 3D are consistent with the quantitative ALP activity findings. In contrast, when stem cells were cultured in powder extracts, all silicon-doped powder extracts enhanced ALP activity on day 14 compared to Si0-PE. However, Si7-PE and Si10-PE inhibited ALP activity on day 3 (Figure S10B). Discrepancies between direct co-culture and indirect culture outcomes may arise from variations in the culture environment, where stem cells co-cultured directly with powders are influenced by factors such as powder morphology and material phases, while cells cultured in powder extracts are solely affected by ion concentrations in the extracts. Nevertheless, both methods indicate that moderate silicon doping promotes osteogenic differentiation of stem cells, whereas excessive silicon doping may impede this process.

In Figure S3, the concentrations of calcium ions and silicon elements in the extracts are presented. The calcium ion concentration across all powder extracts was maintained at approximately 35 ppm, while the silicon element concentration in the extracts increased proportionally with higher levels of silicon doping. Beyond a silicon doping level of 7, there was a rapid escalation in the silicon ion concentration within the extracts, reaching 17 ppm and 20 ppm in the Si7 and Si10 extracts, respectively. The heightened release of silicon ions may potentially account for the observed inhibition of stem cell proliferation (on day 4) and differentiation (on day 3) in the Si7 and Si10 extracts.

In conclusion, the findings from cell culture within the extracts suggest that a moderate level of silicon doping ($\leq$4 mol.%) not only exerts no adverse effects on stem cell proliferation and osteogenic differentiation but may also serve to enhance the process of osteogenic differentiation.

3.3. Physicochemical properties of Si-BCP scaffolds

To further refine and validate the optimal silicon doping concentration, we employed extrusion-based 3D printing to fabricate Si-BCP powder into ceramic scaffolds with a three-dimensional interconnected macroporous architecture. These scaffolds were utilized for culturing both mBMSCs and human umbilical vein endothelial cells (HUVECs) to evaluate their cellular viability, osteogenic differentiation, and vasculogenic potential. The silicon doping levels in the powder extracts was 0, 1, 2, 4, 7, to 10 mol.%. Based on the cellular responses

observed in the culture experiments with the powder extracts, we further optimized the silicon doping concentrations. This optimization included incorporating a 0.5 mol.% silicon-doped BCP powder and adjusting the silicon doping level in the BCP powder from 7 mol.% to 6 mol.% and 8 mol.%. Consequently, the silicon doping concentrations in the BCP powders utilized for scaffold fabrication were systematically adjusted to 0, 0.5, 1, 2, 4, 6, 8, and 10 mol.%.

Due to the propensity of silicon doping to induce the formation of α-TCP phase, as depicted in Fig. 1, the silicon-doped scaffolds were subjected to hydrothermal treatment prior to high-temperature sintering at 1100 °C for a duration of 2 h. Following the hydrothermal treatment, the α-TCP phase underwent complete conversion to HA and β-TCP, resulting in scaffold preforms comprising solely HA and β-TCP phases, as evidenced in Figure S4A. The relative content of HA and β-TCP was approximately 55 wt% and 45 wt%, respectively, as shown in Figure S4C. However, subsequent high-temperature sintering led to alterations in the BCP phase, which resulted in the reappearance of the α-TCP phase, as illustrated in Figure S4B. Additionally, it was observed that higher levels of silicon doping correlated with an augmented α-TCP content. Overall, post-sintering, the HA content within the BCP scaffold exhibited a reduction, while the β-TCP content experienced an increase.

Ion doping induces phase composition changes in BCP, a phenomenon observed in both strontium and magnesium-doped BCP. Research by Xu et al. [33] demonstrates that with increasing strontium doping, the content of β-TCP in strontium-doped BCP significantly rises. For instance, as strontium doping increases from 10 mol.% to 50 mol.%, β-TCP content increases from 24 mol.% to 63 mol.%. Achieving phase stability in strontium-doped BCP with varying strontium doping levels can be challenging, potentially due to excessively high doping concentrations studied. Researchers may choose higher strontium doping levels because of the ion's minimal toxicity threshold and the need for relatively high strontium concentrations to significantly promote osteogenic differentiation of stem cells [34,35]. Similar challenges are observed in magnesium-doped BCP. Lu et al.'s [11] study indicates that increasing magnesium doping from 0 mol.% to 10 mol.% results in β-TCP content increasing from approximately 12 wt% to 100 wt%, highlighting the difficulty in achieving phase stability with varying magnesium doping levels in magnesium-doped BCP. However, Figure S4D indicates that when the silicon doping level was $\leq$4 mol.%, the β-TCP content in the Si-BCP scaffold remained stable at around 60 wt%. This suggests that silicon-doped BCP scaffolds with varying silicon doping levels can achieve relative phase stability when silicon doping is $\leq$ 4 mol.%. Furthermore, subsequent *in vitro* osteogenesis and angiogenesis experiments within this range of silicon doping levels indicate promotion of osteogenic differentiation and vascularization.

The macroscopic morphology and pore structure of the scaffolds were characterized using Si0–S, Si4–S, and Si10–S as examples. Analysis of the SEM images (Figure S5) revealed that all prepared scaffolds exhibited a three-dimensional interconnected macroporous structure, with square through-holes ranging from 400 to 500 μm in size (D2) and lateral pore heights (D3) between 150 and 200 μm. The diameter of the scaffold fibers (D1) was approximately 350 μm (Table S4). Further examination at higher magnifications in the SEM images (Figure S6) indicated that all BCP scaffolds displayed a significant number of micropores resulting from incomplete sintering. Moreover, scaffolds with silicon doping levels $\geq$4 mol.% showed noticeably smaller grain sizes, suggesting that silicon doping could effectively suppress grain growth during the sintering process.

The sintering shrinkage, porosity, and compressive strength of the scaffolds were tested to investigate the influence of silicon doping on the physicochemical properties of BCP ceramic scaffolds, as shown in Figure S7. As the silicon doping level increased from 0 mol.% to 10 mol.%, the sintering shrinkage of Si-BCP scaffolds gradually decreased, while the open porosity increased. Specifically, the open porosity of Si8–S and Si10–S reached up to 80 %. However, this also resulted in lower compressive strength for Si8–S and Si10–S, below 2 MPa. BCP scaffolds
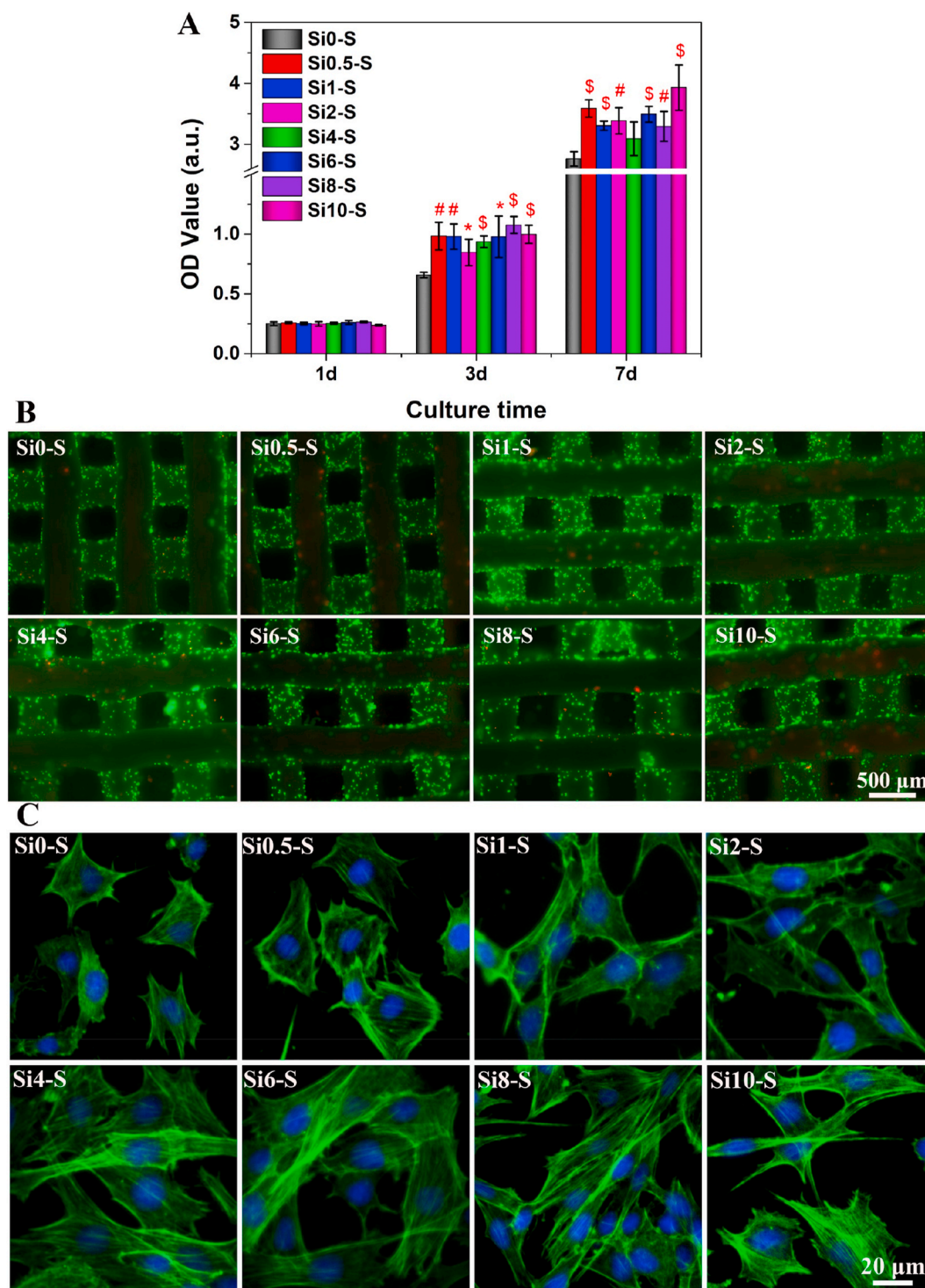
Fig. 4. Biocompatibility of Si-doped BCP scaffolds. Proliferation (A), Live/dead staining (B) and adhesion (C) of mBMSCs cultured on the surfaces of Si-doped BCP scaffolds.

with silicon doping levels equal to or less than 4 mol.% exhibited open porosities between 70 % and 80 %, with compressive strengths exceeding 2 MPa, falling within the range suitable for cancellous bone strength [36], meeting the requirements for material strength in cancellous bone defect repair.

The degradation and ion release of the Si-BCP scaffolds were further analyzed (Figure S8). The findings indicated that during the initial phase of degradation (0–6 weeks), the rate of mass loss of the scaffolds increased significantly, followed by a decrease in the rate during the

later stage of degradation (6–12 weeks). Moreover, silicon doping was found to notably enhance the degradation rate of the scaffolds, particularly in the case of BCP scaffolds with silicon doping levels ≥4 mol.%, which exhibited the highest degradation rate (Figure S8A). In contrast to zinc and magnesium doping, which variably suppress scaffold degradation to different extents [11,17], silicon doping significantly enhances the degradation capability of BCP scaffolds. This enhancement may facilitate more complete bone defect repair by promoting better integration with new bone tissue replacement.
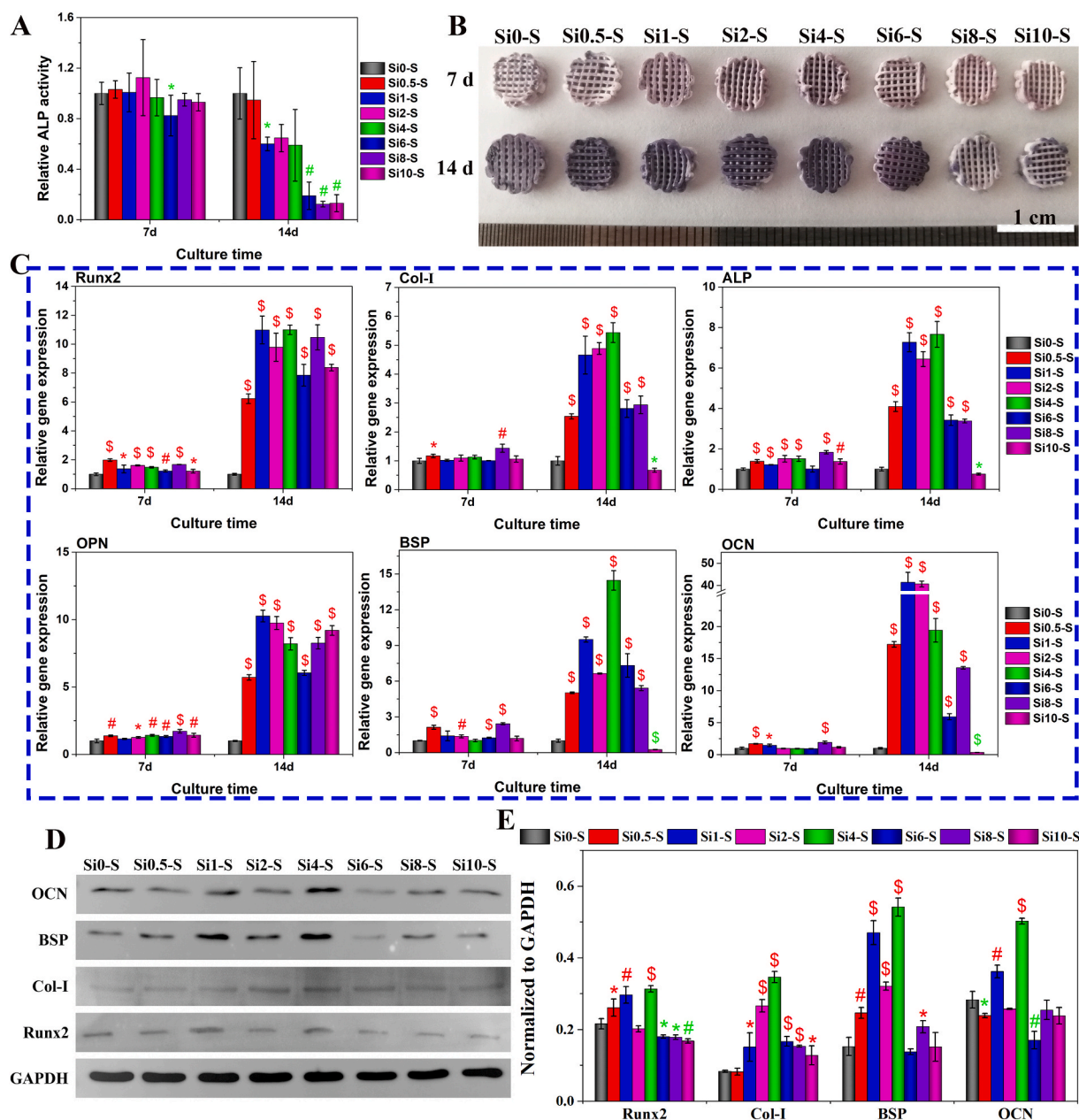
Fig. 5. *In vitro* osteogenic differentiation of mBMSCs cultured on the surface of Si-doped BCP scaffolds. (A) ALP activity; (B) ALP staining images; (C) osteogenesis-related genes expression; (D–E) western blot analysis of osteogenesis-related proteins on day 14 and corresponding quantitative analysis.

As the degradation progressed, the concentrations of released calcium ions and silicon elements from the scaffolds gradually decreased, with the concentration of released silicon elements dropping below 2 ppm by the 12th week (Figure S8B and S8C). Additionally, the mineralization results of the scaffolds in simulated body fluid (SBF) demonstrated that silicon doping induced the formation of mineralization products on the surface of the BCP scaffolds (Figure S9). Specifically, no mineralization products were observed on the surface of Si0–S, while a layer of spherical and block-like mineralization products covered the surfaces of Si1–S and Si2–S. On the surfaces of Si4–S, Si8–S, and Si10–S, flake-shaped mineralization products were formed, which grew further on the surfaces of the spherical and block-like mineralization products.

3.4. In vitro osteogenic activity of Si-BCP scaffold

Stem cells were cultured directly on the surface of the scaffold, and the cell quantity and activity on the scaffold surface were characterized

at different time points after cultivation, as illustrated in Fig. 4. In contrast to culturing in powder extracts and co-culture with powders, all Si-BCP scaffolds exhibited a significant enhancement in promoting stem cell proliferation, particularly at 3 and 7 days of cultivation (Fig. 4A). However, analysis of the live/dead staining results from Fig. 4B revealed that surfaces of scaffolds with higher levels of silicon doping (Si8–S and Si10–S) contained a minor population of red-stained deceased cells.

The morphology of stem cells cultivated on scaffold surfaces was examined by staining the cellular cytoskeleton and visualized using laser scanning confocal microscopy (Fig. 4C). Stem cells cultured on the surfaces of Si0–S, Si0.5-S, and Si10–S exhibited a smaller aspect ratio and smaller spreading area. In contrast, cells cultured on other scaffold surfaces showed a larger aspect ratio, increased spreading area, and extended filamentous pseudopodia. These findings collectively suggest that appropriate silicon doping enhances stem cell adhesion and proliferation on BCP scaffold surfaces.

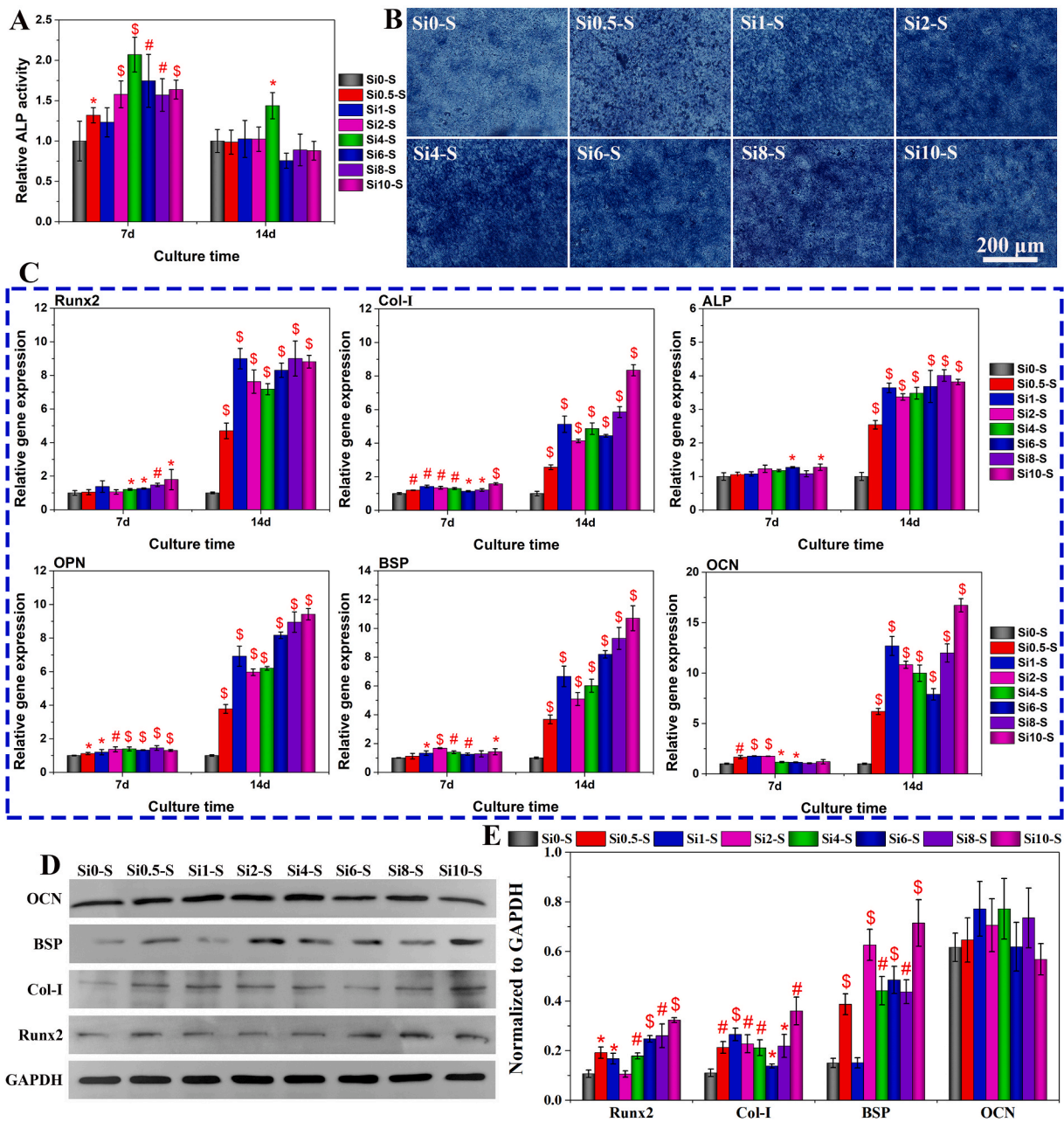The mBMSCs were cultured on the scaffold surfaces for 7 and 14 days

Fig. 6. *In vitro* osteogenic differentiation of mBMSCs cultured in the extracts of Si-doped BCP scaffolds. (A) ALP activity; (B) ALP staining images; (C) osteogenesis-related genes expression; (D–E) western blot analysis of osteogenesis-related proteins on day 14 and corresponding quantitative analysis.

to characterize osteogenic differentiation through ALP activity assays, ALP staining, and analysis of osteogenic marker genes and proteins expression, as depicted in Fig. 5. In Fig. 5A, the ALP activity results demonstrate that silicon-doped scaffolds do not significantly enhance the ALP activity of the adherent stem cells on their surfaces; moreover, after 14 days of culture, these scaffolds even inhibit ALP activity, with the most pronounced inhibitory effect observed in BCP scaffolds with silicon doping levels ≥6 mol.%. Fig. 5B displays ALP staining images, where cells expressing ALP protein appear blue-black, with darker hues indicating higher protein concentrations. The findings reveal that compared to the control group Si0–S, at day 7, Si2–S and Si4–S show enhanced ALP protein expression; by day 14, Si0–S to Si6–S (Si0.5-S, Si1–S, Si2–S, Si4–S, and Si6–S) exhibit increased ALP protein expression. Notably, both Si8–S and Si10–S fail to promote ALP protein expression.

The analysis of osteogenic-related gene expression in Fig. 5C demonstrates that, except for Si10–S, all silicon-doped BCP scaffolds can

upregulate the expression of osteogenic differentiation-related genes, including Runx2, Col-I, ALP, OPN, BSP, and OCN. Among these, Si1–S, Si2–S, and Si4–S exhibit relatively more pronounced enhancing effects. However, Si10–S significantly suppresses the expression of Col-I, ALP, BSP, and OCN at day 14. The expression results of osteogenic proteins (Fig. 5D & E) indicate that scaffolds with silicon doping levels equal to or below 4 mol.% notably promote the expression of osteogenic-related proteins, with Si4–S showing the most prominent enhancing effect. However, scaffolds with higher silicon doping levels (Si6–S, Si8–S, and Si10–S) exhibit less evident promotion of osteogenic protein expression and even suppress the expression of Runx2 protein.

The introduction of silicon led to a suppression of ALP activity in the cultivation of stem cells on the scaffold surfaces (Fig. 5A), a phenomenon distinct from the outcomes observed in stem cells cultured in powder extracts (Figure S10B). It is postulated that the influences on stem cells when cultured on scaffold surfaces are more multifaceted,
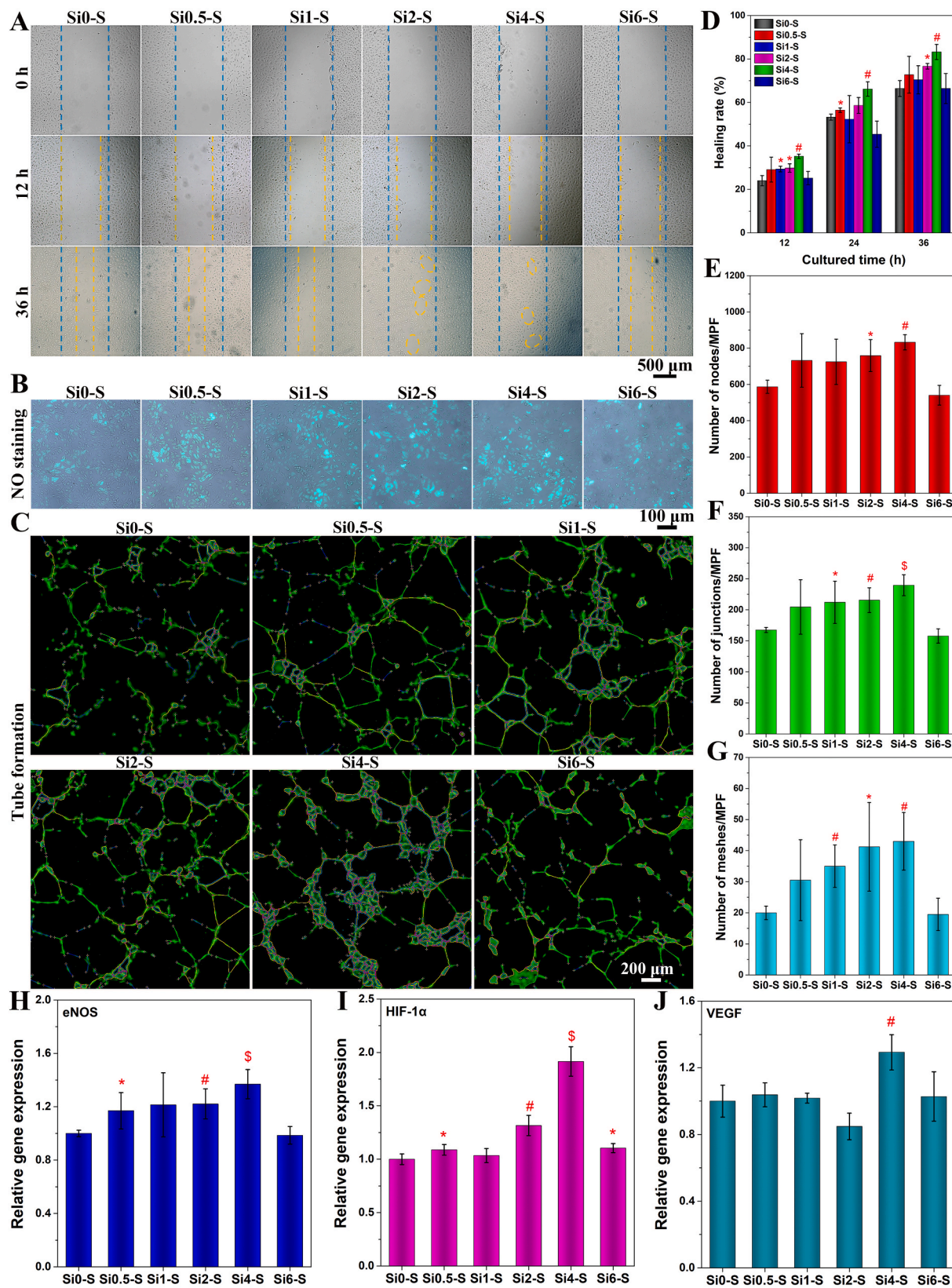
Fig. 7. *In vitro* angiogenesis behaviors of HUVECs cultured in the extracts of Si-doped BCP scaffolds. (A) Scratch assay; (B) NO staining; (C) *in vitro* tube formation assay; (D) cell migration rate; (E) number of nodes; (F) number of junctions; (G) number of meshes; (H) gene expression of eNOS; (I) gene expression of HIF-1α; (J) gene expression of VEGF.

encompassing factors such as phase composition, local ion microenvironment, and scaffold surface morphology. In order to validate this supposition, we undertook to culture stem cells in real-time extracts derived from the scaffolds and characterized the ALP activity, ALP staining, and the expression of osteogenic-related genes and proteins after 7 and 14 days, as presented in Fig. 6.

The results depicted in Fig. 6A reveal that all extracts from silicon-doped scaffolds were able to augment the ALP activity of stem cells at day 7, with the extract from Si4–S demonstrating the most pronounced effect. Notably, the extract from Si4–S continued to significantly elevate the ALP activity of stem cells at day 14. The findings from the ALP staining at day 7 (Fig. 6B) closely mirrored those of the ALP activity, demonstrating that the extracts derived from silicon-doped scaffolds could stimulate the expression of ALP protein in stem cells, with the solution from Si4–S proving to be the most efficacious. The expression of osteogenic-related genes, as shown in Fig. 6C, illustrated that all extracts from silicon-doped scaffolds were capable of upregulating the expression of osteogenic-related genes, with particularly notable effects observed at day 14. Furthermore, the promotion of Col-I, OPN, and BSP at day 14 exhibited a general trend of concentration-dependent enhancement, indicating that higher levels of silicon doping led to a more substantial promoting effect. Similarly, the majority of silicon-doped scaffold extracts significantly enhance the expression of osteogenic-related proteins, including Runx2, Col-I, and BSP, as shown in Fig. 6D & E. The overall trend indicates that higher levels of silicon doping lead to more pronounced promoting effects, although there is no discernible impact on OCN protein expression.

These results suggest that the ion microenvironment established by the degradation of the silicon-doped scaffolds is conducive to the osteogenic differentiation of stem cells. The changes in calcium ion concentration and silicon element concentration in the extracts with soaking time are delineated in Figure S11. Figure S11A illustrates the variation in calcium ion concentration, demonstrating that the concentrations of calcium ions in the extracts of Si0–S, Si0.5-S, Si1–S, and Si2–S increased with soaking time before stabilizing. Conversely, the calcium ion concentrations in the extracts of Si4–S and Si6–S remained relatively stable throughout the soaking process, while those in Si8–S and Si10–S decreased with prolonged soaking time. Figures S11B and S11C depict the real-time concentration and cumulative release concentration of silicon ions, revealing a concentration-dependent relationship, wherein higher doping levels resulted in higher released silicon concentrations. However, it is noteworthy that Si8–S and Si10–S exhibit significantly higher silicon ion release concentrations. This phenomenon is not only associated with silicon doping levels but also with the phase composition of the Si-BCP scaffolds. As depicted in Figure S4D, Si8–S and Si10–S contain a higher proportion of α-TCP, exceeding 20 wt%. Compared to HA and β-TCP, α-TCP degrades more rapidly, thereby contributing to the higher silicon ion release concentrations observed for Si8–S and Si10–S.

The silicon ion concentrations released into the culture medium by Si0.5-S to Si6–S decrease with prolonged immersion time. This trend may be attributed to the silicon ions released mainly from silicon-rich phases distributed on the surface of the calcium phosphate crystals. Research has indicated that some silicon ions do not integrate into the lattice of calcium phosphate but exist as amorphous clusters of silicon-rich phase on the crystal surfaces [37]. In contrast, Si8–S and Si10–S exhibit a trend of initially decreasing and then increasing silicon ion concentrations over time. This behavior is due to the initial release of silicon from the surface silicon-rich phase of the calcium phosphate crystals during the early immersion period (≤4 days). After 4 days, the α-TCP in Si8–S and Si10–S begins to degrade, releasing silicon from the lattice, thereby increasing the silicon ion concentration.

The most prominent alteration in the BCP scaffold pre- and post-silicon doping pertains to its phase composition (Figure S4), showcasing the emergence of α-TCP upon the attainment of a 4 mol.% silicon doping level. Moreover, the abundance of α-TCP escalates concomitantly with the augmentation of silicon doping. Scholarly investigations

underscore the pivotal role of surface stability in orchestrating the osteogenic differentiation cascade in stem cells. Notably, under identical conditions, the degradation rate of α-TCP markedly exceeds that of HA and β-TCP [38]. The prevalence of substantial α-TCP quantities may compromise material surface integrity, thereby impeding the osteoinductive potential of BCP scaffolds harboring heightened silicon doping concentrations, particularly exemplified in Si10–S (Fig. 5).

Upon amalgamating insights from osteogenic differentiation assays encompassing co-cultivation of cells with powders, scaffolds, and extracts of these materials, it emerges that judicious silicon doping holds promise in markedly amplifying the osteogenic differentiation propensity of stem cells. Efficaciously, silicon doping levels ought to be constrained within the ≤6 mol.% ambit, with the zenith of efficacy manifesting at silicon doping levels ranging between 2 and 4 mol.%.

3.5. In vitro angiogenic induction

Based on the findings from *in vitro* osteogenic differentiation experiments, we employed a co-cultivation approach involving ≤6 mol.% silicon-doped BCP scaffolds and HUVECs to investigate the impact of silicon doping on endothelial cell vascularization, as depicted in Fig. 7. It was observed that judicious silicon doping facilitated endothelial cell migration (Fig. 7A and D), with the most pronounced effect observed for scaffolds doped with 4 mol.% silicon, while no discernible promotion was evident when the silicon doping level reached 6 mol.%. Moreover, Si2–S and Si4–S substantially enhanced the expression of NO (Fig. 7B). The morphological outcome of endothelial cell migration under stimulation by scaffold-released ions, as shown in Fig. 7C, revealed a scarcity of interconnected reticular structures with incomplete formation in the case of Si0–S. Conversely, Si1–S, Si2–S, and Si4–S fostered the formation of a more abundant and well-organized reticular network. Semi-quantitative analysis of tubule formation demonstrated that endothelial cell migration induced by Si2–S and Si4–S yielded significantly higher numbers of nodes, junctions, and meshes compared to the control group (Si0–S), with Si4–S exerting the most optimal promoting effect (Fig. 7E–G). Gene expression profiling related to vascularization indicated that Si2–S promoted the expression of eNOS and HIF-1α, whereas Si4–S significantly upregulated the expression of eNOS, HIF-1α, and VEGF. Notably, the influence of Si6–S, with a silicon doping level of 6 mol.%, on the expression of vascular-related genes remained inconspicuous (Fig. 7H–J).

The results of the mBMSCs culture with powder indicate that moderate silicon doping (≤4 mol.%) not only has no detrimental effects on mBMSCs proliferation and osteogenic differentiation, but actually promotes osteogenic differentiation. Both the *in vitro* osteogenic differentiation of mBMSCs cultured on the surface of silicon-doped scaffolds and in real-time extract from the scaffold demonstrate that the ion microenvironment created by the silicon-doped scaffold is conducive to mBMSCs osteogenic differentiation, primarily due to the sustained release of the active element silicon. Furthermore, silicon doping at levels of 2–4 mol.% exhibited the most optimal promotion effect on the *in vitro* osteogenic differentiation of mBMSCs on the silicon-doped BCP scaffold. Similarly, *in vitro* angiogenesis experiments revealed that BCP scaffolds doped with 2 mol.% and 4 mol.% silicon significantly promoted endothelial cell vascularization, with Si4–S demonstrating the most pronounced promoting effect.

Through a comprehensive analysis of the *in vitro* osteogenic and angiogenic experiments, it can be concluded that silicon doping at 2–4 mol.% on the BCP scaffold concurrently enhances mBMSCs osteogenic differentiation and HUVECs vascularization, with the most optimal silicon doping level observed at approximately 4 mol.%.

3.6. In vivo bone regeneration

The Si4–S scaffold, exhibiting optimal *in vitro* promotion of osteogenesis and angiogenesis, was selected for implantation subcutaneously
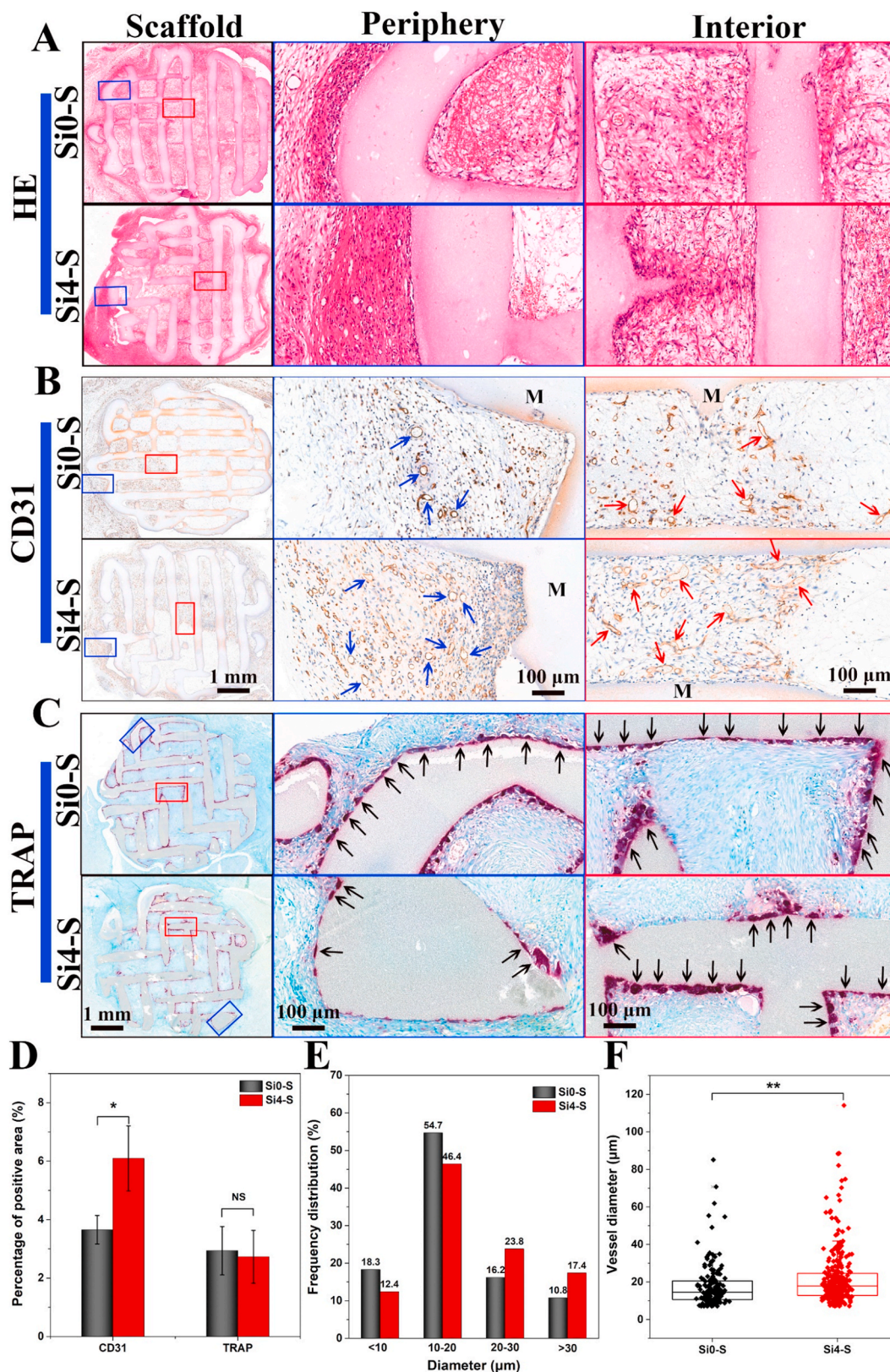
Fig. 8. Histological analysis of Si-doped BCP scaffolds implanted subcutaneously in SD rats for 7 days. HE staining (A), CD31 immunohistochemical staining (B), TRAP staining (C), percentage of CD31 and TRAP positive area (D), distribution (E) and size analysis (F) of new vessel. (Red and blue arrows indicate blood vessels, black arrows indicate TRAP-positive cells).
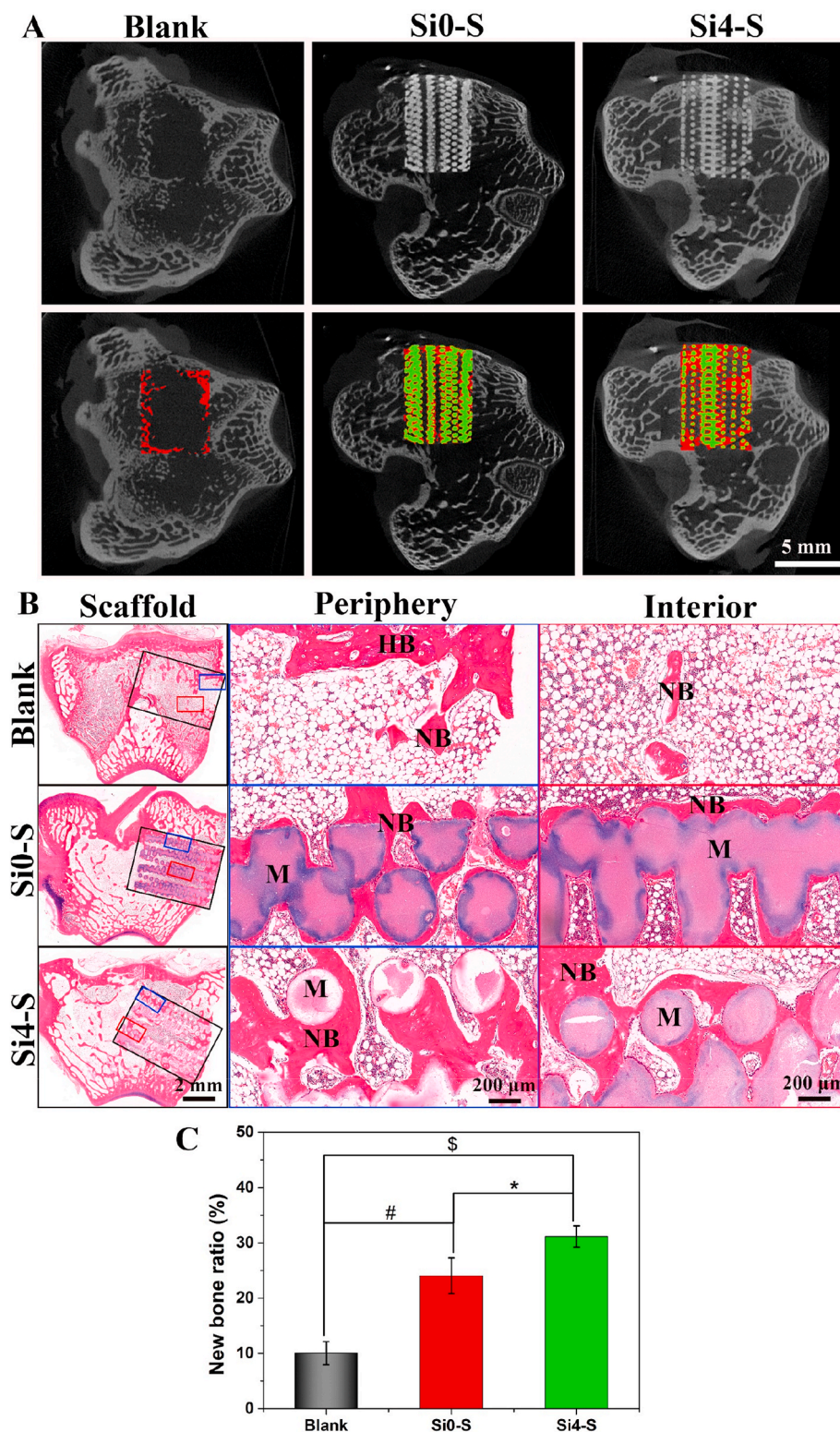
Fig. 9. Micro-CT images (A), HE staining images (B) and the new bone ratio (C) of femur bone defects of rabbits after the implantation of Si-doped BCP scaffolds for 12 weeks. (New bone and residual materials in Micro-CT images were staining in red and green, respectively; "*" $p < 0.05$, "#" $p < 0.01$, "$" $p < 0.001$).

in SD rats and in rabbit femoral defects to further elucidate the influence of silicon doping on the *in vivo* biocompatibility, angiogenic, and osteogenic properties of BCP. The Si0–S scaffold, devoid of silicon doping, was utilized as the control group.

Histological examination using HE staining after seven days of subcutaneous scaffold implantation in SD rats, depicted in Fig. 8A, revealed

substantial tissue infiltration within the scaffold, indicating that the scaffold's three-dimensional interconnected porosity facilitates tissue ingrowth. Notably, there was an absence of inflammatory cell clustering at the scaffold periphery or interior, and no significant fibrous tissue encapsulation was observed. These findings suggest that the prepared BCP scaffold exhibits remarkable biological safety and compatibility.

The CD31 staining results in Fig. 8B reveal that the density of newly formed blood vessels at the edges and within Si4–S is higher compared to Si0–S. Semi-quantitative analysis of vessel area shows a significant increase in the CD31-positive area of Si4–S compared to Si0–S (Fig. 8D). Additionally, the newly formed blood vessels in Si4–S exhibit larger sizes than those in Si0–S (Fig. 8E & F). This indicates that appropriate silicon doping can enhance vascular development and enlargement of BCP scaffolds *in vivo*. The TRAP staining results in Fig. 8C suggest that osteoclasts predominantly reside within the internal pores of both Si0–S and Si4–S, with similar TRAP-positive areas observed in these two scaffold groups (Fig. 8D). This implies that silicon doping does not interfere with the active degradation of BCP scaffolds by osteoclasts *in vivo*.

Following a 12-week period post-implantation of scaffolds measuring 6 mm in diameter and 8 mm in height into rabbit femoral condyle defects, samples were obtained for micro-CT testing, HE staining, and Masson staining to characterize the internal state of new bone formation within the materials, as depicted in Fig. 9. The micro-CT scanning results in Fig. 9A reveal that after 12 weeks of implantation, Si0–S and Si4–S exhibited no significant signs of degradation, with the scaffolds remaining structurally intact. Partial scaffold pores were observed to be filled with new bone, predominantly distributed around the scaffold fibers, aligning with the findings from the HE staining presented in Fig. 9B. Moreover, Si4–S induced the highest quantity of new bone formation, significantly surpassing the new bone volume ratio in both Si0–S and the Blank group (Fig. 9C). The outcomes of Masson staining in Figure S12 demonstrate that the maturity of the newly formed bone at the edges and interior of both Si0–S and Si4–S is on par with that of the host bone. This supports the notion that silicon doping can enhance the capacity of BCP scaffolds to stimulate new bone formation, thereby affirming the potential of Si4–S as a material for bone defect repair.

4. Conclusion

The aim of this study was to investigate the impact of silicon doping on the physicochemical and biological properties of BCP, particularly its osteogenic and angiogenic capabilities, as well as to determine the optimal range and quantity of silicon doping. It was found that the level of silicon doping and the sintering temperature were the primary factors influencing the phase composition. Exceeding 4 mol% silicon doping resulted in the formation of α-TCP, with the content of α-TCP increasing with higher levels of silicon doping and sintering temperature. The presence of α-TCP is advantageous for enhancing the degradation rate of BCP scaffolds, promoting the release of silicon ions, and inducing the formation of mineralization products. However, further increases in the doping level of silicon significantly inhibited the osteogenic differentiation of stem cells and the angiogenic activity of endothelial cells. *In vitro* experimental results indicated that the most favorable range for promoting the osteogenic differentiation of stem cells and the angiogenesis of endothelial cells was between 2 and 4 mol% silicon doping, with an optimal doping level of approximately 4 mol%. *In vivo* experiments confirmed that BCP scaffolds doped with 4 mol% silicon exhibited rapid induction of vascular formation and promoted bone defect repair, demonstrating their potential in clinical bone defect repair. Therefore, this study provides important reference values for enhancing the effectiveness of BCP in bone defect repair.

Data and code availability

The data that support the findings of this study are available from the corresponding author upon reasonable request.

Supplementary information

XRD patterns of Si-doped BCP powder before heat treatment (Figure S1), FTIR spectra at 400-1500 cm^{-1} (A and B) and Raman spectra at 300-1300 cm^{-1} (C and D) of Si-doped BCP treated at 900 °C and 1100 °C (Figure S2), concentration of Ca and Si in the powder extracts of Si-doped BCP powders (Figure S3), phase composition of Si-doped BCP scaffolds (Figure S4), top view and front view of Si-doped BCP scaffolds (Figure S5), free surface and fracture surface of Si-doped BCP scaffolds calcination at 1100 °C for 2 h (Figure S6), sintering shrinkage, open porosity and compressive strength of Si-doped BCP scaffolds (Figure S7), *in vitro* degradation behaviors of Si-doped BCP scaffolds (Figure S8), SEM images of Si-doped BCP scaffolds after immersion in SBF for 2 weeks (Figure S9), cellular response of mBMSCs cultured in Si-doped BCP powder extracts (Figure S10), ions release behaviors of Si-doped BCP incubation in cell culture medium (Figure S11), Masson staining images of Si-doped BCP scaffolds after the implantation for 12 weeks (Figure S12), the ingredients of Si-doped BCPs scaffolds (Table S1), primer sequences of mBMSCs used for RT-PCR in the study (Table S2), primer sequences of HUVECs used for RT-PCR in the study (Table S3), the structure parameters of Si-doped BCP scaffolds (Table S4).

CRediT authorship contribution statement

Teliang Lu: Writing – original draft, Investigation, Formal analysis, Data curation, Conceptualization. **Guohao Li:** Investigation, Formal analysis, Data curation. **Luhui Zhang:** Methodology, Investigation. **Xinyuan Yuan:** Visualization, Validation. **Tingting Wu:** Writing – review & editing, Supervision. **Jiandong Ye:** Writing – review & editing, Supervision, Funding acquisition, Conceptualization.

Declaration of competing interest

The authors declare that they have no known competing financial interests or personal relationships that could have appeared to influence the work reported in this paper.

Data availability

Data will be made available on request.

Appendix A. Supplementary data

Supplementary data to this article can be found online at https://doi.org/10.1016/j.mtbio.2024.101203.

References

[1] N.N. Xue, X.F. Ding, R.Z. Huang, R.H. Jiang, H.Y. Huang, X. Pan, W. Min, J. Chen, J.A. Duan, P. Liu, Y.W. Wang, Bone tissue engineering in the treatment of bone defects, Pharmaceuticals 15 (7) (2022), https://doi.org/10.3390/ph15070879.
[2] A. Brunet, M.A. Goodell, T.A. Rando, Ageing and rejuvenation of tissue stem cells and their niches, Nat. Rev. Mol. Cell Biol. 24 (1) (2023) 45–62, https://doi.org/10.1038/s41580-022-00510-w.
[3] W.B. Zhu, C. Li, M.X. Yao, X.M. Wang, J. Wang, W. Zhang, W. Chen, H.Z. Lv, Advances in osseointegration of biomimetic mineralized collagen and inorganic metal elements of natural bone for bone repair, Regen. Biomater. 10 (2023), https://doi.org/10.1093/rb/rbad030.

[4] A.R. Sousa, J.F. Mano, M.B. Oliveira, Engineering strategies for allogeneic solid tissue acceptance, Trends Mol. Med. 27 (6) (2021) 572–587, https://doi.org/10.1016/j.molmed.2021.03.005.

[5] X.D. Hou, L. Zhang, Z.F. Zhou, X. Luo, T.L. Wang, X.Y. Zhao, B.Q. Lu, F. Chen, L. P. Zheng, Calcium phosphate-based biomaterials for bone repair, J. Funct. Biomater. 13 (4) (2022), https://doi.org/10.3390/jfb13040187.

[6] L.C. Uetanabaro, M. Claudino, R. Zancan, J.C. Zielak, G.P. Garlet, M.R. de Araujo, Osteoconductivity of biphasic calcium phosphate ceramic improves new bone formation: a histologic, histomorphometric, gene expression, and microcomputed tomography study, Int. J. Oral Maxillofac. Implants 35 (1) (2020) 70–78, https://doi.org/10.11607/jomi.7745.

[7] C. Feng, Y.H. Wu, Q.P. Li, T.H. He, Q.L. Cao, X.F. Li, Y.M. Xiao, J.L. Lin, X.D. Zhu, X.D. Zhang, A novel hollow-tube-biphasic-whisker-modified calcium phosphate ceramics with simultaneously enhanced mechanical strength and osteogenic activity, Adv. Funct. Mater. 32 (44) (2022), https://doi.org/10.1002/adfm.202204974.

[8] J.M. Bouler, P. Pilet, O. Gauthier, E. Verron, Biphasic calcium phosphate ceramics for bone reconstruction: a review of biological response, Acta Biomater. 53 (2017) 1–12, https://doi.org/10.1016/j.actbio.2017.01.076.

[9] T. Lu, N. Ma, F. He, Y. Liang, J. Ye, Enhanced osteogenesis and angiogenesis of biphasic calcium phosphate scaffold by synergistic effect of silk fibroin coating and zinc doping, J. Biomater. Appl. 37 (6) (2022) 1007–1017, https://doi.org/10.1177/08853282221124367.

[10] Y. Chen, J. Wang, X.D. Zhu, Z.R. Tang, X. Yang, Y.F. Tan, Y.J. Fan, X.D. Zhang, Enhanced effect of β-tricalcium phosphate phase on neovascularization of porous calcium phosphate ceramics: in vitro and in vivo evidence, Acta Biomater. 11 (2015) 435–448, https://doi.org/10.1016/j.actbio.2014.09.028.

[11] T. Lu, Y. Miao, X. Yuan, Y. Zhang, J. Ye, Adjusting physicochemical and cytological properties of biphasic calcium phosphate by magnesium substitution: an in vitro study, Ceram. Int. 49 (10) (2023) 15588–15598, https://doi.org/10.1016/j.ceramint.2023.01.148.

[12] T.H. He, H.X. Chen, P.X. Liu, H. Shi, X.J. Xu, C. Feng, Y.Y. Wang, X.F. Li, N. Lei, Y. M. Xiao, X.D. Zhu, J.G. Xu, X.D. Zhang, One-step co-doping of ZnO and Zn2+in osteoinductive calcium phosphate ceramics with synergistic antibacterial activity for regenerative repair of infected bone defect, J. Mater. Sci. Technol. 163 (2023) 168–181, https://doi.org/10.1016/j.jmst.2023.04.032.

[13] T.H. He, H.X. Chen, P.X. Liu, H. Shi, X.J. Xu, C. Feng, Y.Y. Wang, X.F. Li, N. Lei, Y. M. Xiao, X.D. Zhu, J.G. Xu, X.D. Zhang, One-step co-doping of ZnO and Zn2+in osteoinductive calcium phosphate ceramics with synergistic antibacterial activity for regenerative repair of infected bone defect, J. Mater. Sci. Technol. 163 (2023) 168–181, https://doi.org/10.1016/j.jmst.2023.04.032.

[14] T. Lu, X. Yuan, L. Zhang, F. He, X. Wang, Y. Zhang, J. Ye, High throughput synthesis and screening of zinc-doped biphasic calcium phosphate for bone regeneration, Appl. Mater. Today 25 (2021) 101225, https://doi.org/10.1016/j.apmt.2021.101225.

[15] D.H. Kim, K.K. Shin, J.S. Jung, H.H. Chun, S.S. Park, J.K. Lee, H.C. Park, S.Y. Yoon, The role of magnesium ion substituted biphasic calcium phosphate spherical micro-scaffolds in osteogenic differentiation of human adipose tissue-derived mesenchymal stem cells, J. Nanosci. Nanotechnol. 15 (8) (2015) 5520–5523, https://doi.org/10.1166/jnn.2015.10463.

[16] Y. Chen, Z.N. Liu, T. Jiang, X.Y. Zou, L. Lei, W.J. Yan, J.W. Yang, B. Li, Strontium-substituted biphasic calcium phosphate microspheres promoted degradation performance and enhanced bone regeneration, J. Biomed. Mater. Res., Part A 108 (4) (2020) 895–905, https://doi.org/10.1002/jbm.a.36867.

[17] T. Lu, X. Yuan, L. Zhang, F. He, X. Wang, J. Ye, Enhancing osteoinduction and bone regeneration of biphasic calcium phosphate scaffold through modulating the balance between pro-osteogenesis and anti-osteoclastogenesis by zinc doping, Mater. Today Chem. 29 (2023) 101410, https://doi.org/10.1016/j.mtchem.2023.101410.

[18] R. Jugdaohsingh, M.R. Calomme, K. Robinson, F. Nielsen, S.H.C. Anderson, P. D'Haese, P. Geusens, N. Loveridge, R.P.H. Thompson, J.J. Powell, Increased longitudinal growth in rats on a silicon-depleted diet, Bone 43 (3) (2008) 596–606, https://doi.org/10.1016/j.bone.2008.04.014.

[19] F.H. Nielsen, Micronutrients in parenteral nutrition: boron, silicon, and fluoride, Gastroenterology 137 (5) (2009) S55–S60, https://doi.org/10.1053/j.gastro.2009.07.072.

[20] Z.H. Ding, Y.Q. Qiao, F. Peng, C. Xia, S. Qian, T. Wang, J.Y. Sun, X.Y. Liu, Si-doped porous TiO2 coatings enhanced in vitro angiogenic behavior of human umbilical vein endothelial cells, Colloids Surf. B Biointerfaces 159 (2017) 493–500, https://doi.org/10.1016/j.colsurfb.2017.08.010.

[21] H. Li, J. Chang, Bioactive silicate materials stimulate angiogenesis in fibroblast and endothelial cell co-culture system through paracrine effect, Acta Biomater. 9 (6) (2013) 6981–6991, https://doi.org/10.1016/j.actbio.2013.02.014.

[22] H.W. Kim, Y.J. Kim, Effect of silicon or cerium doping on the anti-inflammatory activity of biphasic calcium phosphate scaffolds for bone regeneration, Prog. Biomater. 11 (4) (2022) 421–430, https://doi.org/10.1007/s40204-022-00206-6.

[23] D.C. Chen, G.H. Chen, X. Zhang, J.T. Chen, J.M. Li, K.L. Kang, W.T. He, Y.H. Kong, L.L. Wu, B. Su, K. Zhao, D.W. Si, X.T. Wang, Fabrication and in vitro evaluation of 3D printed porous silicate substituted calcium phosphate scaffolds for bone tissue engineering, Biotechnol. Bioeng. 119 (11) (2022) 3297–3310, https://doi.org/10.1002/bit.28202.

[24] G. Dong, Y.X. Zheng, L.Y. He, G. Wu, C.L. Deng, The effect of silicon doping on the transformation of amorphous calcium phosphate to silicon-substituted α-tricalcium phosphate by heat treatment, Ceram. Int. 42 (1) (2016) 883–890, https://doi.org/10.1016/j.ceramint.2015.09.013.

[25] C.M. Botelho, R.A. Brooks, S.M. Best, M.A. Lopes, J.D. Santos, N. Rushton, W. Bonfield, Human osteoblast response to silicon-substituted hydroxyapatite, J. Biomed. Mater. Res., Part A 79A (3) (2006) 723–730, https://doi.org/10.1002/jbm.a.30806.

[26] W.C.M. Duivenvoorden, A. Middleton, S.D. Kinrade, Divergent effects of orthosilicic acid and dimethylsilanediol on cell survival and adhesion in human osteoblast-like cells, J. Trace Elem. Med. Biol. 22 (3) (2008) 215–223, https://doi.org/10.1016/j.jtemb.2008.02.001.

[27] P. Gillespie, G. Wu, M. Sayer, M.J. Stott, Si complexes in calcium phosphate biomaterials, J. Mater. Sci. Mater. Med. 21 (1) (2010) 99–108, https://doi.org/10.1007/s10856-009-3852-8.

[28] R. Astala, L. Calderín, X. Yin, M.J. Stott, Ab initio simulation of Si-doped hydroxyapatite, Chem. Mater. 18 (2) (2006) 413–422, https://doi.org/10.1021/cm051989x.

[29] X.L. Yin, M.J. Stott, Theoretical insights into bone grafting silicon-stabilized α-tricalcium phosphate -: art. no. 024709, J. Chem. Phys. 122 (2) (2005), https://doi.org/10.1063/1.1829995.

[30] G. Gasqueres, C. Bonhomme, J. Maquet, F. Babonneau, S. Hayakawa, T. Kanaya, A. Osaka, Revisiting silicate substituted hydroxyapatite by solid-state NMR, Magn. Reson. Chem. 46 (4) (2008) 342–346, https://doi.org/10.1002/mrc.2109.

[31] W.T. Kong, K. Zhao, C.X. Gao, P.Z. Zhu, Synthesis and characterization of carbonated hydroxyapatite with layered structure, Mater. Lett. 255 (2019), https://doi.org/10.1016/j.matlet.2019.126552.

[32] E.A. Taylor, C.J. Mileti, S. Ganesan, J.H. Kim, E. Donnelly, Measures of bone mineral carbonate content and mineral maturity/crystallinity for FT-IR and Raman spectroscopic imaging differentially relate to physical-chemical properties of carbonate-substituted hydroxyapatite, Calcif. Tissue Int. 109 (1) (2021) 77–91, https://doi.org/10.1007/s00223-021-00825-4.

[33] Y. Xu, Z. Geng, Z. Gao, X. Zhuo, B. Li, Z. Cui, S. Zhu, Y. Liang, Z. Li, X. Yang, Effects of both Sr and Mg substitution on compositions of biphasic calcium phosphate derived from hydrothermal method, Int. J. Appl. Ceram. Technol. 15 (1) (2018) 210–222, https://doi.org/10.1111/ijac.12771.

[34] M. Huang, R.G. Hill, S.C.F. Rawlinson, Strontium (Sr) elicits odontogenic differentiation of human dental pulp stem cells (hDPSCs): a therapeutic role for Sr in dentine repair? Acta Biomater. 38 (2016) 201–211, https://doi.org/10.1016/j.actbio.2016.04.037.

[35] B. Kruppke, C. Heinemann, A.S. Wagner, J. Farack, S. Wenisch, H.P. Wiesmann, T. Hanke, Strontium ions promote in vitro human bone marrow stromal cell proliferation and differentiation in calcium-lacking media, Dev. Growth Differ. 61 (2) (2019) 166–175, https://doi.org/10.1111/dgd.12588.

[36] T. Lu, S. Feng, F. He, J. Ye, Enhanced osteogenesis of honeycomb beta-tricalcium phosphate scaffold by construction of interconnected pore structure: an in vivo study, J. Biomed. Mater. Res., Part A 108 (3) (2020) 645–653, https://doi.org/10.1002/jbm.a.36844.

[37] N. Douard, R. Detsch, R. Chotard-Ghodsnia, C. Damia, U. Deisinger, E. Champion, Processing, physico-chemical characterisation and in vitro evaluation of silicon containing beta-tricalcium phosphate ceramics, Mater. Sci. Eng. C 31 (3) (2011) 531–539, https://doi.org/10.1016/j.msec.2010.11.008.

[38] H. Rojbani, M. Nyan, K. Ohya, S. Kasugai, Evaluation of the osteoconductivity of α-tricalcium phosphate, β-tricalcium phosphate, and hydroxyapatite combined with or without simvastatin in rat calvarial defect, J. Biomed. Mater. Res., Part A 98A (4) (2011) 488–498, https://doi.org/10.1002/jbm.a.33117.